Holography-Based Target Localization and Health Monitoring Technique Using UHF Tags Array

Aline Eid, *Student Member, IEEE*, Jiang Zhu, *Senior Member, IEEE*, Luzhou Xu, *Senior Member, IEEE*, Jimmy G. D. Hester, and Manos M. Tentzeris, *Fellow, IEEE*

***Abstract*—Radio technologies are appealing for unobtrusive and remote monitoring of human activities. Radar-based human activity recognition proves to be a success, for example, Project Soli developed by Google. However, it is expensive to scale up for multiuser environments. In this article, we propose a solution—the HoloTag system—which circumvents the multichannel-radar scaling problem through the use of a quasivirtual ultralow-cost UHF RFID array over which a holographic projection of its environment is measured and used to both localize and monitor the health of several targets. The method is first described in detail, before the image reconstruction process, employing known beamforming algorithms—Delay & Sum, and Capon—is shown and its scaling properties simulated. Then, the idiosyncrasies of the implementation of HoloTag using low-cost off-the-shelf hardware are explained, before its ability to simultaneously measure the breathing rates and positions of multiple real and synthetic targets with accuracies of better than 0.8 bpm and 20 cm is demonstrated.**

***Index Terms*—Healthcare, holography, radio frequency identification (RFID), target localization, ultrahigh frequency (UHF), vital signs.**

I. Introduction

AMBIENT computing has been gaining momentum to be one of the most impactful technological developments for the next decade. At its core, it requires the devices to interact with the environments and users seamlessly and ubiquitously. Our era is witnessing a rapid development in the field of human activity monitoring, indoor localization, and health care systems. The ability to monitor vital signs in real time can, to a great extent, help with disease early diagnosis and prevention [1], [2]. Breathing has been recently used to encode information, allowing people with severe paralysis to communicate with others [3]. In addition, combining the vital signs monitoring systems with localization capabilities can answer questions about the physical and mental health of a person. Vital signs monitoring systems can be realized using either intrusive or contactless approaches [4]. For applications, such as elderly care, intrusive techniques [5], [6] can be cumbersome, obstructed by clothes, or even sparsely used due to negligence. Therefore, for continuous long-term monitoring, contactless techniques constitute the best candidate with the least interference on the patients' daily activities [7]. However, contactless technologies generally rely on the observation of signals generated by patients in their immediate environment. It is, nevertheless, beneficial to scale such systems to large coverage areas in order to reduce costs. This introduces the necessity to differentiate between the breathing and heart rates (HRs) and to match the measured signals to their associated targets. Radar systems have demonstrated high accuracy localization and real-time vital sign monitoring in scenarios involving multiple targets [8], [9]. However, those solutions require expensive, dedicated systems with performance, costs, and power consumptions scaling quasi-proportionally with the bandwidth and with the number of transmitters and receivers and, therefore, with angular and radial resolutions. A potential low-cost and low-complexity alternative to the employment of such dedicated hardware could lie in the well-established-and-perfected passive ultrahigh frequency (UHF) radio-frequency identification (RFID) technology. RFID readers are readily available in the market and can be deployed in the indoor environment along with compact, ultralow-cost, and batteryless tags.

Nevertheless, the limited bandwidth allowable by the federal communications commission (FCC) (26 MHz at UHF frequencies)—leading to frequency-based ranging resolutions and accuracies worse than several meters—superficially seem to spell the doom of UHF wireless devices for the aforementioned applications. An alternative to sampling in the frequency (and, therefore, radial) domain lies in the potential ability to sample in the spatial domain, as is commonly implemented in antenna arrays to determine Angles of Arrival (AoAs). However, such a design choice is complex, expensive, and quickly becomes unmanageably large in the UHF band, thereby defeating the purpose of the use of UHF RFID. In lieu of such large static systems, synthetic aperture radar (SAR) schemes—which reduce the complexity of the wireless system—have been proposed to create large virtual arrays [10], [11]. Despite their advantages, their itinerant nature introduces mechanical challenges and is unbecoming in most environments. An ideal solution to this problem would

Manuscript received January 9, 2021; revised March 20, 2021; accepted April 2, 2021. Date of publication April 7, 2021; date of current version September 23, 2021. This work was supported by the Google Internship Program. *(Corresponding authors: Jiang Zhu; Luzhou Xu.)*

This work involved human subjects or animals in its research. The authors confirm that all human/animal subject research procedures and protocols are exempt from review board approval.

Aline Eid is with the Device and Service Product Area, Google LLC, Mountain View, CA 94043 USA, and also with the Department of Electrical and Computer Engineering, Georgia Institute of Technology, Atlanta, GA 30332 USA.

Jiang Zhu and Luzhou Xu are with the Device and Service Product Area, Google LLC, Mountain View, CA 94043 USA (e-mail: jiangzhu@google.com; lzxu@google.com).

Jimmy G. D. Hester is with Atheraxon, Atlanta, GA, USA, and also with the Department of Electrical and Computer Engineering, Georgia Institute of Technology, Atlanta, GA 30332 USA.

Manos M. Tentzeris is with the Department of Electrical and Computer Engineering, Georgia Institute of Technology, Atlanta, GA 30332 USA.

Digital Object Identifier 10.1109/JIOT.2021.3071693

give birth to static yet scalable, low-cost, and large-aperture real or virtual arrays. This is what the proposed solution enables by employing a groundbreaking method consisting in the holographic projection of envrionmental targets over ultralow-cost UHF RFID tag arrays.

The main contributions of the HoloTag system can be summarized as follows.

1) First UHF RFID implementation utilizing holographic imaging for combined target localization and breathing rate (BR) extraction.
2) First holography-based system implementing beamforming using a static, passive array of UHF tags. The implementation relies on a single transmitter antenna and a single receiver antenna coupled with an array of tags. The implementation requires no movement of equipment for area scanning compared to similar approaches such as SAR.
3) The technique relies on cross-circularly-polarized tags-RX antenna instead of traditional linearly polarized (LP) tags to help suppress the direct communication path between the tags and the receiver antenna and improve the signal-to-noise ratio (SNR) of signals reflecting off the human body.
4) This technology relies on a reduced number of tags for accurate localization and differentiation between at least two targets. Improving the performance and localization accuracy of the system comes at a very low-cost and minor complexity. By solely adding more tags to the array and upgrading the information in the software, one can achieve more robust and more accurate localization measurements.
5) The system introduces a synthetic target (ST) that can be modulated at any breathing frequency to emulate a real human without suffering from the inconsistencies and imperfections of a living target. This addition played a significant role in the optimization of the hardware setup and processing of the data before experimenting with real humans, as well as facilitating multiusers scenarios.

II. Related Work

The literature contains a wide variety of approaches that are tailored toward specific needs and applications. This could range from the sole real time monitoring of vital signs to the precise and accurate localization and to general gestures extraction.

Multiple radar solutions have been proposed in the literature using techniques, such as frequency-modulated continuous wave (FMCW) [12], [13], ultrawideband (UWB) [8], [9], [14], Doppler [15], [16], and WiFi [17], [18]. For example, Zhang *et al.* [9] proposed MTrack, a system equipped with 2 GHz of bandwidth, one transmitter antenna, and 16 receiver antennas, which is capable of tracking people's trajectories and extracting the breathing and HRs of static targets under multiperson scenarios. This article relies on AoA and ToF in addition to implementing a path selection algorithm to suppress interference from dynamic multipaths. [8] for example, can track users' breathing and HRs with a median accuracy of 99% up to a distance of 8 m away from the device. The high penetration and range resolution observed in these systems come at a high cost when compared to commercial radio systems. Besides the signal being very sensitive to any motion in the environment, the extraction of vital signs using radar technologies suffers from increased size, cost and power consumption with the increase in bandwidth and with the number of TX/RX channels. The specialized hardware and array of antennas utilized are not commercially available and are not practical for deployment in a home or clinical environment for long term sensing.

On the lower end of the complexity and cost scale lie UHF systems, with limited bandwidths and, consequently, radial resolutions. Despite this limitation, researchers have, seemingly, managed to leverage UHF technology for accurate target localization and/or breathing and HRs detection. Zhao *et al.* [7] proposed a contactless breathing and HR monitoring system based on UHF commercial off-the-shelf (COTS) RFID devices. Although the proposed system is easy to implement in addition to being low cost, their multiuser solution is highly dependent on the LOS and the distance between the user and the tag. Also, since target localization is not implemented, it is impossible to match each target to their BR and HR. On the other hand, some efforts have solely focused on target localization using COTS UHF RFID tags combined in some cases with imaging techniques without the extraction of any vital signs. Ma *et al.* [19] demonstrated target localization with 0.24-m median error using an impractically large two TX/RX reader-antennas system and a set of 50 tags placed on two orthogonal walls. Unlike [19] that takes advantage of both received signal strength indicator (RSSI) and phase information, [20] and [21] rely solely on the RSSI information to accurately localize targets in indoor environments. Their hardware consists of four reader antennas and 30 RFID tags. While these systems achieve good indoor localization accuracies, their hardware is relatively large and complex and their implementation is limited to localization. In addition, these reported experiments were conducted in large and empty rooms that suffer from minimal multipath compared to small rooms and cluttered environments.

III. HoloTag System

A. Theory of Operation

The principles of holography—practice of making holograms or 3-D images—have been applied not only with light waves but also with microwaves and acoustic waves. Holographic methods are well known in the area of ultrasonic and radar imaging [22]–[24] and have found several applications at microwave frequencies such as biomedical imaging [25], concealed weapon detection [26], [27], and RFID tags localization [28]–[32]. The basic concept behind holography is to correlate a signature measured by multiple radar/reader units with a reference signature generated at every possible location. This estimator, ideally, results in a maximum at the position of the tested target and at a infinitesimal value otherwise. All holography-based target localization implementations at UHF presented to date in the literature involve the

movement of the hardware (reader antenna or tags) along a known trajectory to create a virtual array capable of scanning a specific area.

This technique applied in those works on UHF hardware [28], [29], [32]–[34] is inspired by SAR that leverages the motion of the radar antenna over a target region to provide fine range measurement and resolution. Holography-based tag localization involves two major steps: 1) measurement or simulation and storage of the backscattered signals (phase and/or RSSI information) at each possible location and 2) hologram generation and tag localization.

In this work, we combine holography and beamforming techniques to localize and monitor the health of real targets (RTs) (human beings) in a novel unprecedented way. With a static array of UHF RFID tags, one transmitter and one receiver (co-located for compactness) antennas with known locations, two beamforming techniques—one conventional and the other adaptive—were applied based on propagation path model to estimate the positions of one or multiple targets.

Several well-known methods can be used to address the problem of estimating the direction of arrival (DOA) which, as we will see, can readily be extended to holopgrahic 2-D localization. Beamforming—enabled by an array of antennas—acts as a spatial filter to transmit and receive signals to and from a specific direction in the presence of interference and noise. In order to form a beam in a desired direction, the signal corresponding to each element in the array is usually multiplied by a certain weight, then all signals are combined coherently resulting in a pattern being maximized in the desired direction and attenuated in all other unwanted directions. Conventional and adaptive beamforming approaches correspond to different choices of the weighting vector w. A commonly used beamforming technique is the delay & sum (DS) in the frequency domain. The weights for this method are found by calculating the delay encountered in each tag due to path difference, so that the outputs of spatially distributed tags are coherently summed to improve signal reception in the presence of noise. Another technique, called "Capon" and belonging to the "adaptive beamforming" class, relies on data-dependent weights, that will be calculated using a steering vector and a covariance matrix, defined in the following equations. The steering vector or array manifold vector used in both beamforming techniques is based on the path propagation model presented in Fig. 1. There is a specific propagation phase associated with each tag defined by the triangle path starting with the TX antenna to Tag 1 with phase ϕ_1', then from Tag 1 to Target with phase ϕ_1'' and finally from Target to RX antenna with phase ϕ_1'''. Assuming this single significant path signal, the signal received by the radar $x(t)$ can be expressed at any time t as

$$x(t) = a(\theta)s(t) + n(t) \tag{1}$$

where $a(\theta)$ is the steering vector associated with the path, $s(t)$ is the desired signal portion of $x(t)$ received by the N tags, where N is the number of tags, and $n(t)$ is the noise.

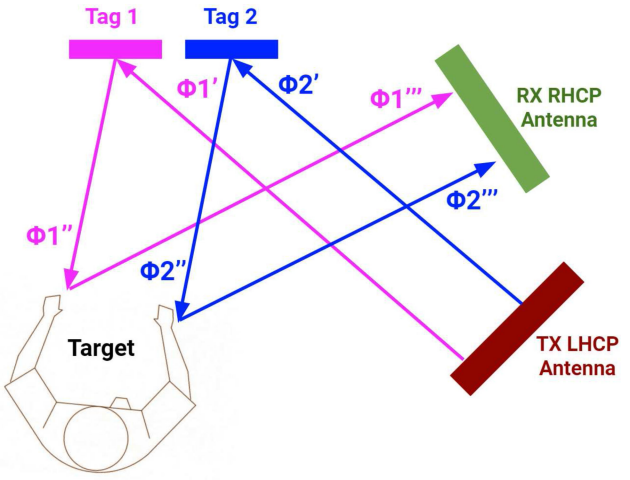

Fig. 1. Schematic describing the propagation path model between tags, target, and TX and RX antennas.

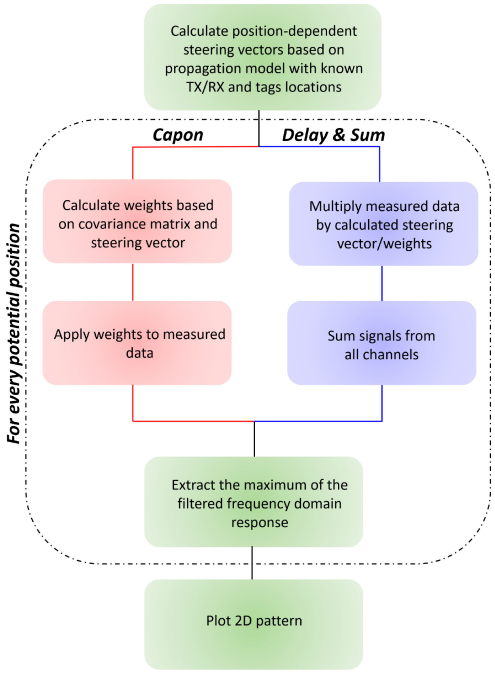

Fig. 2. Flowchart describing the steps leading to target localization using DS and Capon beamforming algorithms.

A steering vector is formed by calculating the phase shifts associated with each tag as shown in the following equation:

$$a(\theta) = \left[e^{-j(\phi_n)}\right] \tag{2}$$

where ϕ_n is the total phase shift associated with tag n—as described in the following equation—with n being the tag number:

$$\phi_n = \phi_n' + \phi_n'' + \phi_n''' \tag{3}$$

with ϕ_n', ϕ_n'', and ϕ_n''' representing the propagation phase from TX to Tag, Tag to Target, and Target to RX, respectively.

The phases are calculated from the distances using the following equation:

$$\phi = \frac{2\pi d}{\lambda} \tag{4}$$

where d and λ are the distance and wavelength, respectively.

In order to estimate $s(t)$, two methods were implemented, whereby $y(t)$—an estimator of $s(t)$—was obtained by multiplying the measured signal by the calculated weights

$$y(t) = wx(t). \tag{5}$$

As previously mentioned, the weights associated with the DS method are data-independent and can be calculated by simply finding the conjugate of the steering vector $a(\theta)$ and multiplying it by the signal $x(t)$ as follows:

$$w_{\mathrm{DS}} = \overline{a(\theta)} \tag{6}$$

where w_{DS} are the weights associated with DS. On the other hand, the weights associated with the Capon algorithm rely on both the calculated steering vector and covariance matrix obtained based on the measured data

$$R_{xx} = \frac{1}{L}\sum_{t=1}^{L} x(t)x^H(t) \tag{7}$$

where R_{xx}, $x^H(t)$ and L are the received signal covariance matrix, the Hermitian (or complex-conjugate transpose) of the received signal, and the number of samples, respectively.

By solving the constraint optimization problem for the weight vector, detailed in [35], we obtain

$$w_C = \frac{R_{xx}^{-1}a(\theta)}{a^H(\theta)R_{xx}^{-1}a(\theta)} \tag{8}$$

where w_C and R_{xx}^{-1} are the weights associated with Capon and the inverse covariance matrix, respectively.

It should be noted that the aforementioned methods grew out of far-field array-based signal processing efforts. However, the operating context of the technology introduced in this work presents—and, even, unlocks—the opportunity for positioning in two (or three) spatial dimensions rather than in a univariate angular space. For this purpose, it is necessary to adapt these methods to tackle this 2-D problem. This can, trivially, be done by simply substituting $a(x, y)$ or $a(x, y, z)$ for $a(\theta)$. The generated estimator then seamlessly adopts the same number of dimensions as the steering vector. The position of the target can then be calculated based on an estimator computed using the following process.

1) Using the calculated weights for the position (x, y), compute $y(t)$ using (5).
2) Apply a standard nonuniform fast fourier transform (NUFFT) of $y(t)$ to obtain $\mathcal{Y}(f)$.
3) Extract the magnitude of the frequency point of $\mathcal{Y}(f)$ corresponding to the breathing signal, which is used as the value of the position estimator $Y(x, y)$ at that position.

Repeating these steps for every position results in the 2-D interference patterns presented later in this article for position estimation.

B. Implementation

1) Introducing the Hardware: The RFID system used in this work is composed of the Impinj Speedway R420 reader, one TX left hand circularly polarized (LHCP) antenna (S9028PCL with gain 9 dBi), one RX right hand circularly polarized (RHCP) antenna (S9028PCR with gain 9 dBi) and LHCP tags. Unlike previous implementations [5], [7], [19] that use COTS LP tags with the CP reader antennas, our previous work [36] proposed a solution that attenuates the direct communication link between the tag and the reader antennas—a major challenge when indirect links reflecting on targets carry the needed information—by implementing a cross-circular polarization between the reader antenna and the tag. Fig. 3 helps illustrate the difference in the signals' paths in scenarios using LP tags and CP tags, in a cluttered environment. With the LP tag, the reader antenna receives signals predominantly from the tag, in addition to attenuated reflections from targets and obstacles in the environment. With a CP tag of opposite polarization from that of the reader, the direct communication between the tag and the reader suffers more than 30 dB of attenuation due to polarization mismatch, while signals passing through the target and carrying body movement information will flip polarization and be received by the reader. The proposed approach in [36] has demonstrated an improved SNR and spatial sensitivity compared to conventional LP tags. It is worth mentioning that the same phenomenon has been exploited to design a miniaturized radar antenna array [37]. In [36], a spiral antenna is used for the CP tag, yielding a wide CP bandwidth. For the purpose of illustrating the underlying methodology, the same CP tag antenna is chosen in this article. It should be noted that there are plenty of choices of miniaturized CP antennas for the specific use case, for example, from the classic patch antenna [37] to the metamaterial-loaded one [38].

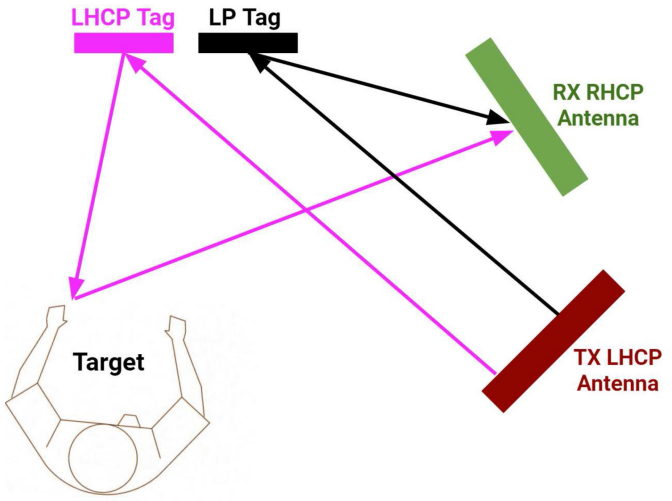

Fig. 3. Schematic describing the difference in propagation path for a CP tag versus an LP tag.

While one reader antenna is usually used as both TX and RX with the impinj reader, we have proposed a different method that reduces the crosstalk between the transmitting and receiving channels and, thus, increases the receiver's sensitivity. To enable two separate TX and RX channels on the reader, a circulator was used to channel the transmitted power through an LHCP antenna (same polarization as the tags), while the received signal from the target (that switched polarization from

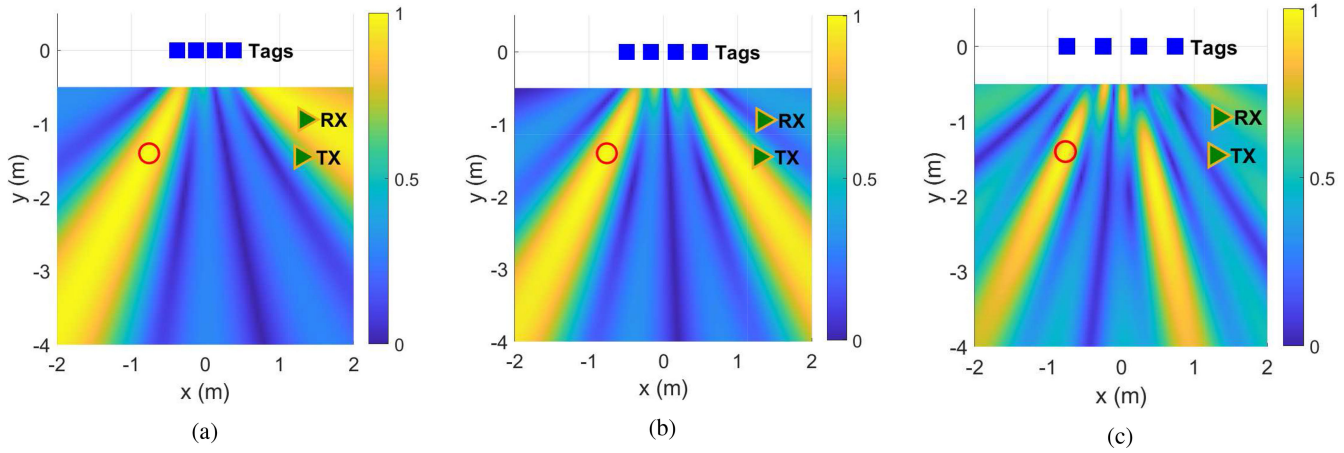

Fig. 4. Simulated 2-D interference patterns showing the effect of the separation distance d (center to center) between the tags for a target located at (-0.76 m, -1.4 m) (marked with the red circle) and a four-tags scenario: (a) $d = 3\lambda/4$, (b) $d = \lambda$, and (c) $d = 3\lambda/2$.

LHCP to RHCP through reflection on body) is received by the RHCP antenna and channeled back to the reader through the circulator. In this scenario, the tags can be turned on at larger distances since they are powered by antennas of the same polarization while the received signal of opposite polarization—due to its reflection on the target—is collected by an antenna of its same polarization. It should be noted that the interrogation range can be further extended with the implementation of multiple reader antennas, as shown in [39], or with the tuning of the current CP tag design to achieve higher gains.

In order to understand and better visualize the effect of the number of tags in the array and the separation d between them, we implemented holographic-based simulations using the delay and sum algorithm. For this purpose, the code was fed with the following information: the positions of the tags, TX/RX reader antenna, target to aim toward, number of tags, and separation d between them. The algorithm then calculated the paths for every possible position within the grid, that would translate to a phase, as detailed in the previous section. The resulting 2-D interference pattern, relying on the Delay and Sum algorithm, maximizes the response in the known direction of the target and minimizes it in all other directions. Since the plotted values were normalized by the maximum, the scale ranges from 0 to 1 and is unitless. It should be noted that the target location is provided to the code in the simulation only, to observe the beamforming behavior. Similar to the phased arrays design, the spacing between the elements—in our case, tags—depicts the performance of the array and can introduce coupling and side lobes if not well chosen. It is well known that the separation between the elements of an array must be less than $\lambda/2$ to eliminate side lobes, however, since the center-to-center distance between our tags is almost $\lambda/2$ at 900 MHz, it is impossible to achieve this separation without inducing high coupling between the elements. Therefore, constrained with the CP tag's dimensions, we have simulated three distances: 1) $3\lambda/4$; 2) λ; and 3) $3\lambda/2$. Fig. 4 shows the simulated interference pattern of four tags for the three aforementioned separations, where TX, RX, and target's locations remained unaltered. The target was set to position (-0.76 m, -1.4 m) marked with a red circle on the pattern. It was observed that although the side lobes appear in all three cases—expected due to $d > \lambda/2$—their interference with the RT location becomes more apparent as the distance between the elements increases. Therefore, the shortest distance ($3\lambda/4$ or 25 cm) at which coupling between elements is prevented and side lobes effect was reduced was chosen to be used in the system. The effect of the number of tags was studied next. In this simulation, similar to the previous setup, the target was set to (-0.76 m, -1.4 m) and TX/RX and tags locations were unchanged. Three scenarios were considered: 1) two; 2) four; and 3) eight tags. Similar to antenna arrays, where the angular resolution increases (spacing being equal) as the number of elements increase, the tags arrays setup demonstrated the same behavior, as shown in Fig. 5. The simulated 2-D interference patterns display the increased resolution and precision in position estimation as the number of tags increases. Since the middle implementation enables a good compromise between a decent accuracy and a low number of elements, four tags were adopted for the first measurement campaign.

2) Synthetic Tag Design: As previously mentioned, the goal from this technology is to be able to localize real human targets in small indoor environments, such as clinics waiting rooms, offices, or any room inside a house. For this purpose, we have chosen a small, cluttered office space, surrounded by concrete walls and glass windows, comprised of a large wooden table, chairs, and a large TV. In order to test the system and isolate its properties from the errors introduced by imperfect human targets, a ST—that can mimic the BR of a real person—was designed. The ST was realized with a basic tag design that involves an antenna and a switch capable of receiving, modulating and re-emitting a synthetic breathing signal. Modulated at any desired BR, the tag acts like a perfect human target that we define later in the experiments as "ST." The Times-7 A8060 (LP) Indoor RFID Antenna with moderate gain of 5 dBi and 110° of azimuth beamwidth was chosen. A field effect transistor (FET) CE3520K3 was used as a switch connected to the antenna to form the tag as shown in Fig. 6, and modulated

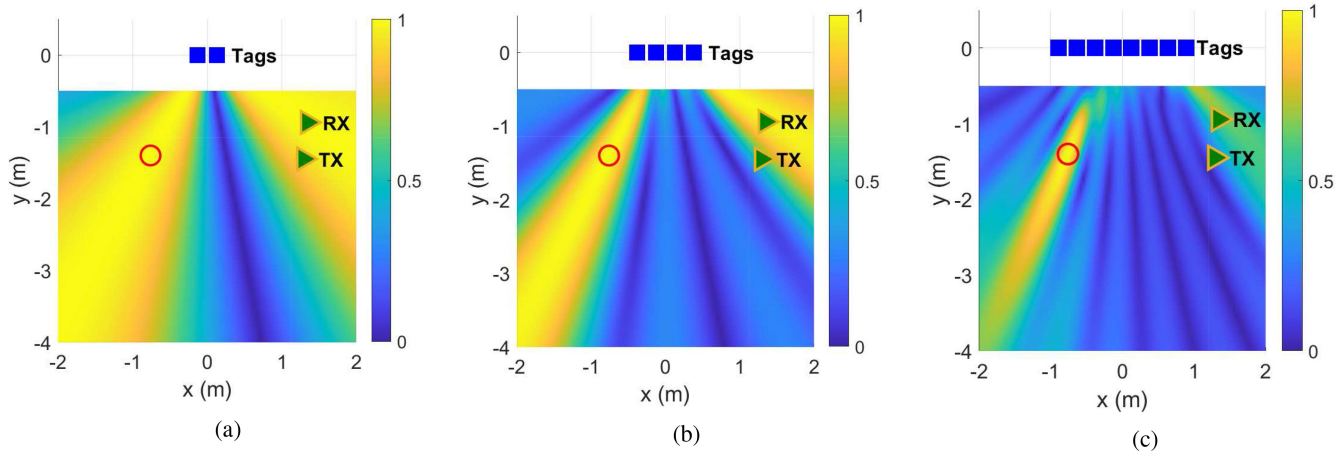

Fig. 5. Simulated 2-D interference patterns showing the effect of the number of tags on the localization accuracy for a target located at (−0.76 m, −1.4 m) (marked with the red circle) and a separation $d = 3\lambda/4$: (a) two tags, (b) four tags, and (c) eight tags.

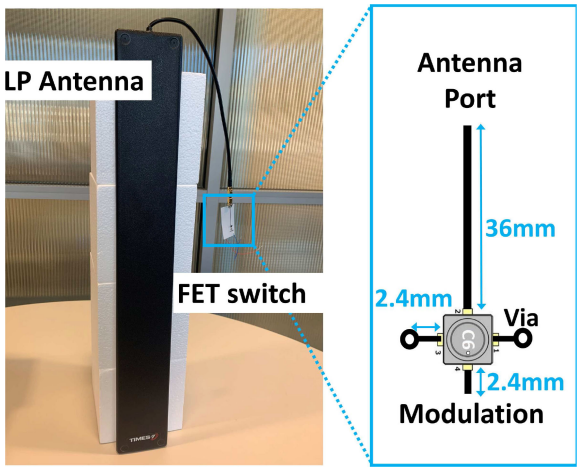

Fig. 6. Photograph of the synthetic tag composed of an LP antenna and FET switch with layout included.

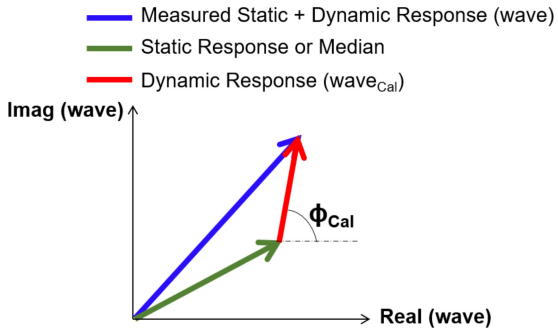

Fig. 7. Expressing the measured wave as the sum of two complex components: one static and one dynamic.

by binary phase-shift keying (BPSK) at any chosen synthetic BR rate. The synthetic tag was used to test and optimize the system as well as assist in the multitarget scenarios.

C. Data Preprocessing

The determination of positions from the aggregated signals backscattered by individual tags of the array relies almost exclusively on phase information, as is the case for antenna arrays. Nevertheless, the individual responses received by the reader combine signals transmitted through the direct LOS channel, as well as that produced by series of scattering events over the environment surrounding the system. The proposed approach employs the *dynamic* nature of vital signals—for instance, the periodicity of the breathing cycle—to filter static interference out of the measured responses. The electromagnetic theory teaches that the downconverted responses (in terms of both its magnitude and Phase) received by the reader can be expressed as a sum of individual *waves*, each contributed by a different element in the set of relevant paths connecting the TX and RX antennas via tag scattering. This wave is thus defined

$$\text{wave} = \sqrt{\text{RSSI}}\, e^{j\Phi} \tag{9}$$

where RSSI and Φ are the signal strength indicator and the phase of the signal.

These concepts lead to the understanding that the signals measured by the reader can be expressed as the complex sum of a static, clutter-produced component and of a dynamic component produced by the living target, as depicted in Fig. 7. It is clear that the extraction of the phase of the dynamic signal; therefore, necessitates accurate averaged and instant estimations of *both* the RSSI and the Phase.

In order to extract the needed information, the raw data—collected during measurement—has to undergo one calibration step. Due to the inherent nature of the Impinj reader that follows the frequency hopping spread spectrum (FHSS) method—where the reader hops between 50 channels (from 902.75 to 927.25 MHz) every 10 s—it is difficult to extract information from the raw data, as shown in Fig. 8. The calibrated wave signal per channel i denoted by "wave$_{\text{Cal},i}$" was calculated by removing the "median" value of *wave* for each channel independently, as follows:

$$\begin{aligned}\text{wave}_{\text{Cal},i} = &\sqrt{\text{RSSI}_i}\, e^{j(\Phi_{i,2}+\text{median}(\Phi_{i,1}/2))} \\ &- \sqrt{\text{median}(\text{RSSI}_i)}\, e^{j(\text{median}(\Phi_{i,1}/2))}\end{aligned} \tag{10}$$

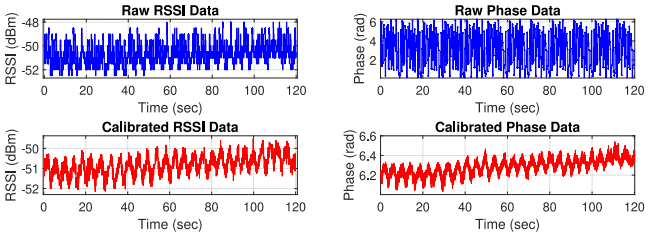

(a) (b)

Fig. 8. Raw measured versus calibrated data. (a) RSSI data in (dBm). (b) Phase data in (rad).

where RSSI_i is the RSSI of channel i, $\Phi_{i,1}$ and $\Phi_{i,2}$ are defined as

$$\Phi_{i,1} = \text{unwrap}(\Phi_i) \tag{11}$$

where Φ_i the phase for channel i

$$\Phi_{i,2} = \text{unwrap}\big(\Phi_{i,1} - \text{median}\big(\Phi_{i,1}/2\big)\big). \tag{12}$$

These steps were necessary because the raw phase data outputted by the reader ranges from 0° to 360° and is ambiguous by 180°. Finally, wave_{Cal} is obtained by aggregating all the individually calibrated data from all channels at their respective sampling times. This process not only removes, to a great extent, the variations due to frequency hopping but also substracts the static response of the environment, thereby only leaving behind the contributions of dynamic targets.

Fig. 8 shows the importance of RSSI and phase data calibration and elimination of frequency hopping effect for target information extraction. The BR of the target in this specific experiment can be easily calculated from the plot. The calibrated RSSI data are obtained by computing the squared magnitude of the calibrated wave as follows:

$$\text{RSSI}_{\text{Cal}} = |\text{wave}_{\text{Cal}}|^2. \tag{13}$$

The calibrated phase data are obtained as follows:

$$\Phi_{Cal} = \text{unwrap}(\angle \text{wave}_{\text{Cal}}). \tag{14}$$

It should be noted that the sampling times for the time domain measurements taken by the reader are somewhat random and nonuniform: each sampling time for a given tag corresponds to the interrogation time of that particular tag which, due to the slotted ALOHA time-division process implemented by the reader, creates a stochastic time series. As a consequence, all frequency information relied upon in this work was calculated using a standard NUFFT algorithm.

IV. Experimental Evaluation

The testing area shown in Fig. 9 is a small conference room filled with chairs and surrounded by glass windows and concrete walls with metal separations. The system was first tested with four tags placed on the same plane for DOA and BR estimation. The next step involved the addition of four extra tags on the orthogonal plane to the first set of tags while the TX and RX antenna positions remained unaltered.

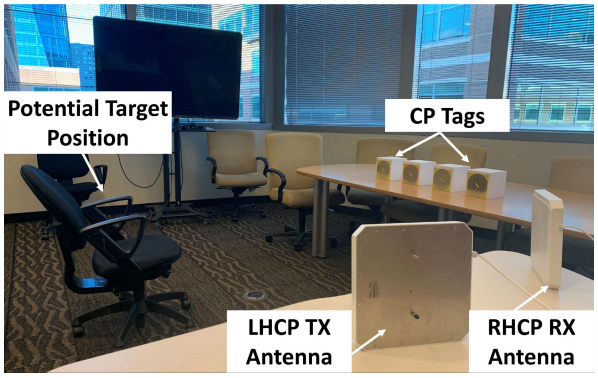

Fig. 9. Photograph of the setup implementing four linear tags array for target DOA estimation and BR extraction.

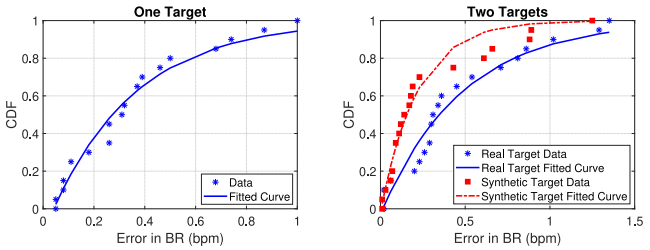

(a) (b)

Fig. 10. Errors in estimated BR in bpm for (a) one target and (b) two targets scenarios.

A. Scenario of Linear Four-Tags Array

For this setup, the TX antenna was placed on a table at position (1.3 m, −1.45 m) facing the four tags centered at (0, 0) situated on a wooden table and separated by $3\lambda/4$ (25 cm). The RX antenna, located at (1.35 m, −0.94 m) was oriented toward the space, where the target could be located. The space in which the target was moving is approximately 4 m by 3 m. Forty 2-min experiments were first collected with this setup, where 20 involved a single target and the other 20 included two targets: one real and the other synthetic. During those experiments, the targets BR was changed between 6 and 30 bpm following a metronome for precision and comparison with the ground truth. The targets locations' were changed for every experiment and positions of targets were often switched in the two-target scenario. The BR information was extracted from the filtered frequency-domain data obtained by first applying the NUFFT, followed by a bandpass filter including, frequencies from 0.08 to 1 Hz (corresponding to 4.5–60 bpm to cover abnormal breathing). Finally, a peak search was used to locate the peak with the maximum amplitude that corresponds to the breathing frequency. The BR was then compared to the ground-truth set by the metronome resulting in the cumulative distribution function (CDF) plots shown in Fig. 10. It can be seen that the maximum error—calculated in the presence of one target—is 1 bpm while the error remains less than 0.4 bpm for more 60% of the measurements. Similarly, in the presence of two targets, the error remains less than 0.5 bpm for 65% of the times with a RT and 75% for the ST. This is indeed expected since the ST's rate is controlled and does not suffer from the imperfections and irregular breathing that occur

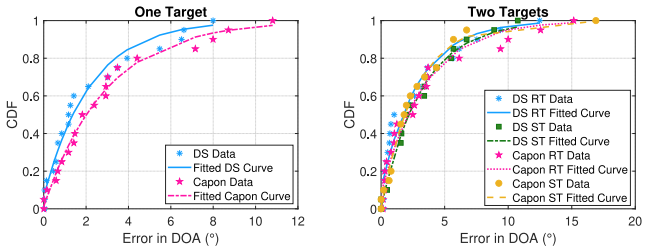

(a) (b)

Fig. 11. Errors in estimated DOA in degrees for (a) one target and (b) two targets (RT and ST) scenarios using DS (DS) and Capon algorithms.

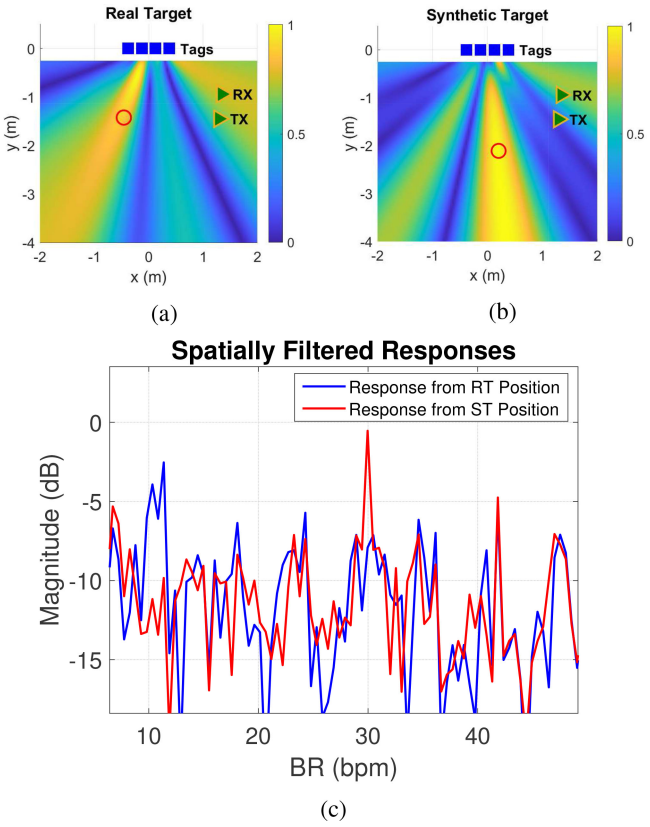

(a) (b) (c)

Fig. 12. Measured responses for two targets (Real + Synthetic) scenario: (a) measured 2-D pattern for RT, (b) measured 2-D pattern for ST, (c) measured spatially filtered responses for both targets identifying their BRs depending on their location.

with a real human. The collected data were then processed using both DS and Capon algorithms to extract the DOA. The targets' locations were converted to angular positions using the following formula:

$$\theta_{\text{Actual}} = \tan^{-1}\left(\frac{x}{y}\right)180°/\pi \tag{15}$$

where θ_{Actual} is the actual angular position of the target with respect to the tags, x and y are the horizontal and vertical positions.

The calculated actual angle was then compared to the measured estimated angle extracted from the 2-D pattern and the error was calculated as follows:

$$E_\theta = |\theta_{\text{Actual}} - \theta_{\text{Estimated}}| * \left|\cos\left(\frac{\theta_{\text{Actual}} + \theta_{\text{Estimated}}}{2}\right)\right| \tag{16}$$

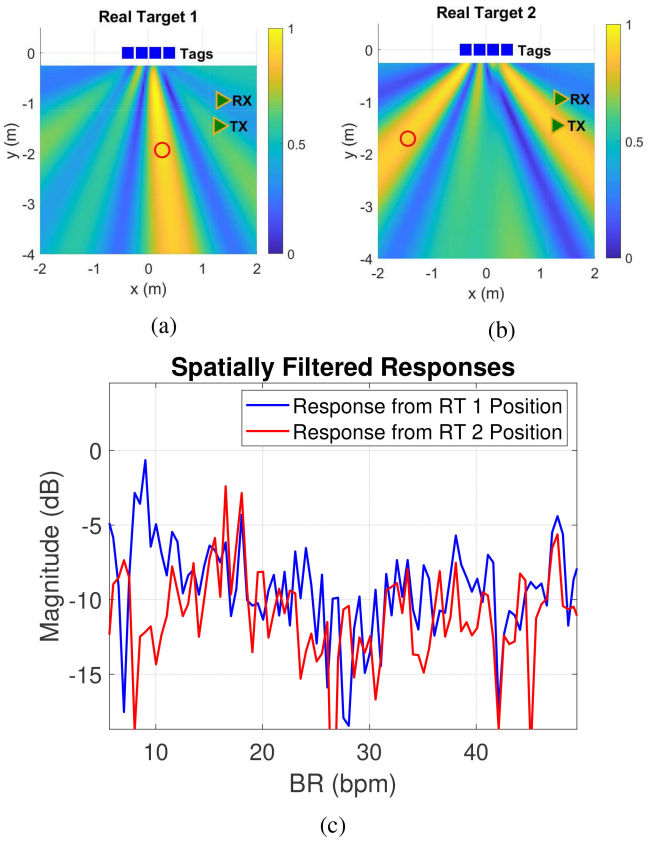

(a) (b) (c)

Fig. 13. Measured responses for two RTs scenario: (a) measured 2-D pattern for real target 1 (RT 1), (b) measured 2-D pattern for real target 2 (RT 2), and (c) measured spatially filtered responses for both targets identifying their BRs depending on their location.

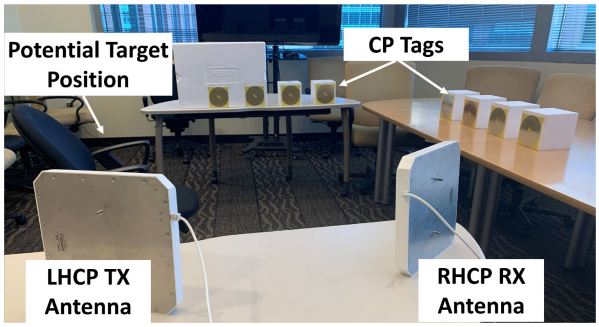

Fig. 14. Photograph of the setup implementing eight tags divided into two orthogonal arrays for target 2-D localization and BR extraction.

where E_θ is the calculated error in DOA, and $\theta_{\text{Estimated}}$ is the estimated DOA extracted from the measured data. The cosine factor allows for the direct comparison of errors measured over the entire angular space: errors increase as the target moves away from normal, due to the $\propto \sin\theta$ nature of the phase differences measured by consecutive array elements.

The CDF plots for DOA estimation shown in Fig. 11(a) resulting from this system—equipped with only four tags—show that the proposed technology is capable of estimating the DOA of one target with an error less than 8° and 11° using DS and Capon, respectively. In the case of two targets, shown in Fig. 11(b), the error remains below 12° with DS and 17° with Capon with a superiority in angular localization accuracy of the ST.

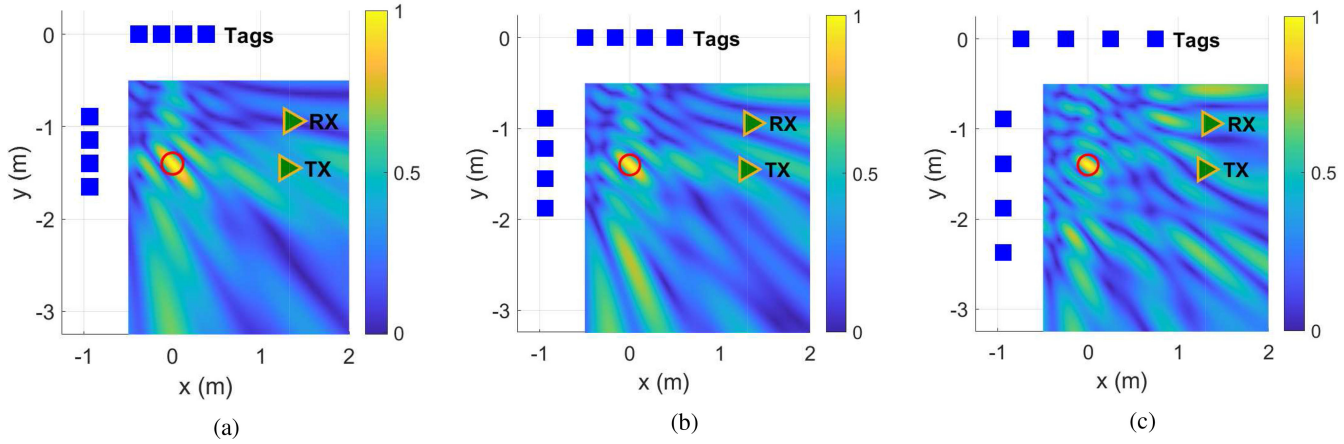

Fig. 15. Simulated 2-D interference patterns showing the effect of the separation distance d (center to center) between the tags for a target located at (0 m, −1.4 m) (marked with the red circle) and a eight tags scenario: (a) $d = 3\lambda/4$, (b) $d = \lambda$, and (c) $d = 3\lambda/2$.

As highlighted in the introduction, the main capability of the proposed approach lies in the ability of localizing two targets and differentiating their BRs using a simple, static and low-cost system. Figs. 12 and 13 display two examples out of many conducted experiments with two targets.

Fig. 12(a) and (b) displays the measured 2-D patterns for a RT located at (0.45 m, −1.4 m) and a ST at (0.2 m, −2.1 m), respectively. It should be noted that although the patterns show each target individually, the experiment was conducted in the presence of both targets. Those patterns are the results of the two maxima observed in the filtered frequency domain that are theoretically associated with the BR of each target. The red circle placed on the plot shows the known location of the target. In order to determine the DOA from the measurement, the mean values of all the points in a given direction were calculated for the entire 2-D pattern. Finally, the mean yielding the highest value was selected as the measured target direction. As seen in Fig. 12(a) and (b) the exact and predicted angles, i.e., red circle and yellow beam, coincide, demonstrating the ability to successfully locate the angular position of the target. Since plotting the patterns using the two peaks in the frequency domain is not enough to correlate each target with their BR, it is important to plot the frequency-domain response corresponding to each measured location: i.e., "spatially filtered."

Fig. 12(c) displaying the two spatially filtered responses, proves the ability to identify each target's BR based on their location. In this scenario, the RT had a BR of around 11.5 bpm while the ST was set at a modulation rate of 0.5 Hz or 30 bpm. Experiments involving two RTs were also conducted and Fig. 13 is one example displaying the localization as well as the differentiation in BR based on the estimated location. In this experiment, the first RT was located at (0.2 m, −1.93 m) while the second RT was at (−1.5 m, −1.7 m). As detailed earlier, the measured target's direction was determined by finding the direction of maximum mean value over the entire pattern. The measured 2-D patterns shown in Fig. 13(a) and (b) demonstrate the ability to correctly localize the two RTs. It should be highlighted that the localization of targets located at high angles relative to the tags array is often accompanied with the presence of side lobes as seen on the edge of Fig. 13(b) in the direction of the TX and RX antennas. This is justified by the separation between of the tags that exceeds $\lambda/2$ as previously displayed in Fig. 4. Followed by the 2-D patterns are the spatially filtered responses reflecting the BR of each target based on their location, where target 1 had a BR of 9 bpm while target 2 was breathing at a rate of approximately 17 bpm. It should be noted that the experiments shown in Figs. 12 and 13 did not use a metronome to control the RT's BR, in order to emulate realistic operating scenarios. Since it is challenging to maintain a perfect BR over the entire testing period, the peaks in the frequency domain appear disrupted unlike clean peaks resulting from the controlled ST experiments.

B. Scenario of Eight Orthogonal Tags Array

After demonstrating the capabilities of one set of four linear tags array in achieving a good localization in terms of DOA, another set, similarly composed of four tags spaced by $3\lambda/4$, were placed on the plane orthogonal to the first set, as shown in Fig. 14. Such an implementation results in the combination of two beams (each coming from one set of four tags), thereby resulting ideally in a small detection area on the 2-D pattern that would enable high accuracy (x, y) localization. In order to better illustrate the resulting beam, the setup composed of the eight tags was simulated using DS algorithm and 2-D patterns were plotted for different tag separation as shown in Fig. 15. It should be noted that the simulated tag separation involved only each set of linear tags. The horizontal and vertical separation between the two sets of tags was unchanged in those experiments. Similar to Fig. 4, the simulated center to center distances were $3\lambda/4$, λ, and $3\lambda/2$. It can be shown from Fig. 15 that the presence of secondary locations become more apparent with the increase of the separation between the linear array elements. Although the formed beam appears to be more defined in Fig. 15(c) for a separation $d = 3\lambda/2$ [similar to how the beam was more directive in Fig. 4(c)], side lobes appear in the form of secondary positions that could result in false targets localization. Therefore, the

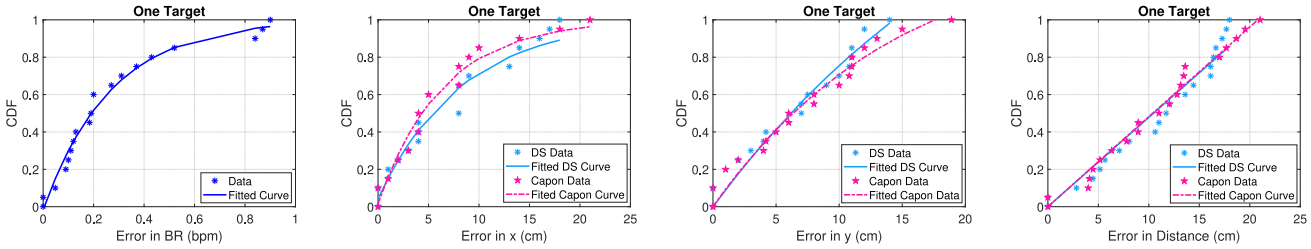

(a) (b) (c) (d)

Fig. 16. Errors in estimated position and BR of one target for the eight orthogonal tags array scenario. (a) Error in BR (in bpm). (b) Error in localization in x (in cm) with DS and Capon. (c) Error in localization in y (in cm) with DS and Capon. (d) Error in localization in total distance (in cm) with DS and Capon.

same separation $d = 3\lambda/4$, shown in Fig. 15(a), chosen for the four tags experiments was also picked for the the new setup as a compromise between good localization accuracy and minimal secondary positions. In order to validate the operation of the orthogonal setup, 20 2-min experiments were conducted with a single RT, while the BR and the location were changed for every experiment. The CDF plots shown in Fig. 16 were obtained by subtracting the actual BR, x and y positions from the predicted ones, respectively. Fig. 16(a) shows that a BR error less than 0.9 bpm is observed in the new orthogonal setup. The errors in (x, y) localization, presented in Figs. 16(b) and (c), demonstrate the capabilities of this setup to localize a target with an error less than 18 and 14 cm in x and y, respectively, using DS, and 21 and 19 cm in x and y, respectively, using Capon. The localization error in terms of distance was also calculated resulting in the CDF plot shown in Fig. 16(d), displaying an error less than 18 cm with DS and 21 cm with Capon, over all experiments. This proposed technology—with only eight tags—outperforms previously proposed UHF-based localization techniques that require at least 20 to 30 tags to enable (x, y) localization [19]–[21]. An example of the results obtained from the conducted experiments is shown in Fig. 17. In this experiment, the target was located at $(-0.05$ m, -2.03 m), while the TX and RX were located at (1.3 m, -1.45 m) and (1.35 m, -0.94 m), respectively, with constant positions in all the experiments. The simulated and measured 2-D patterns shown in Fig. 17 validate the proper operation of the system and demonstrate its ability to accurately localize the target within few cm of error. It is important to highlight that the secondary position appearing in the measured 2-D pattern in the direction of the RX antenna is mainly due to secondary side lobes resulting from the separation between the tags. Some potential solutions would be to tune the distance d between the tags, window the data and/or apply different techniques other than Capon or DS.

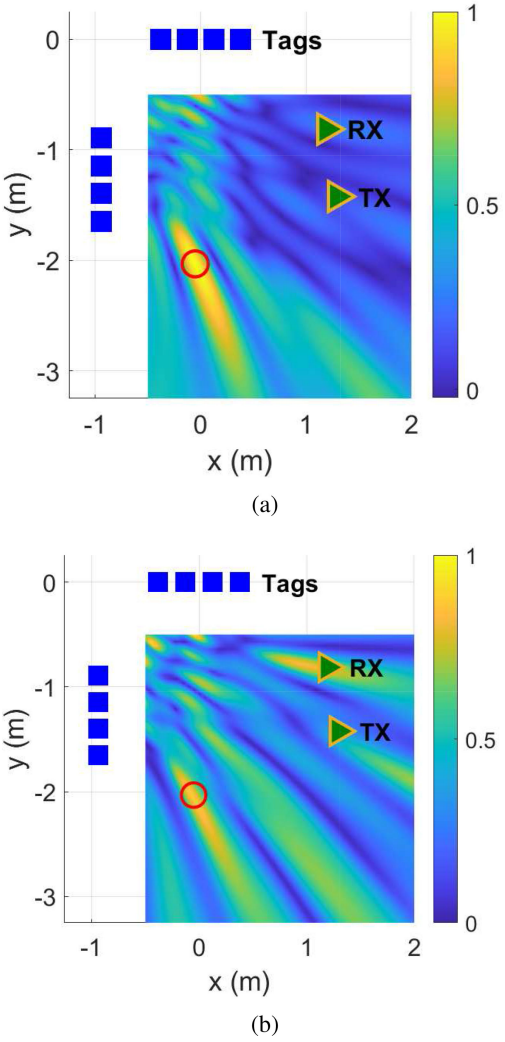

(a)

(b)

Fig. 17. Localization of RT located at $(-0.05$ m, -2.03 m) using eight tags. (a) Simulated 2-D pattern. (b) Measured 2-D pattern.

V. Conclusion

The HoloTag system presented in this article allows the implementation of large-aperture and, therefore, high-resolution imaging and health-monitoring systems which can scale at virtually no cost using OTS UHF RFID readers and tags. While only moderate in scale in the experiments presented here, its scaling and integration into living and clinical environments, along with its support through the use of machine learning algorithms may set the foundation for the advent of affordable "smart-room" systems with ultrahigh-resolution awareness for the support of patient care and home automation.

References

[1] M. S. Mahmud, H. Wang, A. M. Esfar-E-Alam, and H. Fang, "A wireless health monitoring system using mobile phone accessories," *IEEE Internet Things J.*, vol. 4, no. 6, pp. 2009–2018, Dec. 2017.

[2] M. C. Caccami, M. Y. S. Mulla, C. Occhiuzzi, C. Di Natale, and G. Marrocco, "Design and experimentation of a batteryless on-skin RFID graphene-oxide sensor for the monitoring and discrimination of breath anomalies," *IEEE Sensors J.*, vol. 18, no. 21, pp. 8893–8901, Nov. 2018.

[3] Q. Wang, J. Zhao, S. Xu, and R. Wang, "ReType: Your breath tells your mind!" *IEEE Internet Things J.*, early access, Feb. 5, 2021, doi: 10.1109/JIOT.2021.3057474.

[4] X. Liu, J. Yin, Y. Liu, S. Zhang, S. Guo, and K. Wang, "Vital signs monitoring with RFID: Opportunities and challenges," *IEEE Netw.*, vol. 33, no. 4, pp. 126–132, Jul./Aug. 2019.

[5] Y. Hou, Y. Wang, and Y. Zheng, "TagBreathe: Monitor breathing with commodity RFID systems," in *Proc. IEEE 37th Int. Conf. Distrib. Comput. Syst. (ICDCS)*, 2017, pp. 404–413.

[6] C. Wang, L. Xie, W. Wang, Y. Chen, Y. Bu, and S. Lu, "RF-ECG: Heart rate variability assessment based on cots RFID tag array," *Proc. ACM Interact. Mobile Wearable Ubiquitous Technol.*, vol. 2, no. 2, pp. 1–26, 2018.

[7] R. Zhao, D. Wang, Q. Zhang, H. Chen, and A. Huang, "CRH: A contactless respiration and heartbeat monitoring system with COTS RFID tags," in *Proc. 15th Annu. IEEE Int. Conf. Sens. Commun. Netw. (SECON)*, 2018, pp. 1–9.

[8] F. Adib, H. Mao, Z. Kabelac, D. Katabi, and R. C. Miller, "Smart homes that monitor breathing and heart rate," in *Proc. 33rd Annu. ACM Conf. Human Factors Comput. Syst.*, 2015, pp. 837–846.

[9] D. Zhang, Y. Hu, and Y. Chen, "MTrack: Tracking multi-person moving trajectories and vital signs with radio signals," *IEEE Internet Things J.*, vol. 8, no. 5, pp. 3904–3914, Mar. 2021.

[10] F. Bernardini *et al.*, "Particle swarm optimization in SAR-based method enabling real-time 3D positioning of UHF-RFID tags," *IEEE J. Radio Freq. Identification*, vol. 4, no. 4, pp. 300–313, Dec. 2020.

[11] R. Zhao, D. Wang, Q. Zhang, H. Chen, and H. Xu, "PEC: Synthetic aperture RFID localization with aperture position error compensation," in *Proc. 16th Annu. IEEE Int. Conf. Sens. Commun. Netw. (SECON)*, 2019, pp. 1–9.

[12] J. Lien *et al.*, "Soli: Ubiquitous gesture sensing with millimeter wave radar," *ACM Trans. Graph.*, vol. 35, no. 4, pp. 1–19, 2016.

[13] I. Nasr *et al.*, "A highly integrated 60 GHz 6-channel transceiver with antenna in package for smart sensing and short-range communications," *IEEE J. Solid-State Circuits*, vol. 51, no. 9, pp. 2066–2076, Sep. 2016.

[14] L. Anitori, A. de Jong, and F. Nennie, "FMCW radar for life-sign detection," in *Proc. IEEE Radar Conf.*, 2009, pp. 1–6.

[15] A. D. Droitcour, O. Boric-Lubecke, and G. T. A. Kovacs, "Signal-to-noise ratio in doppler radar system for heart and respiratory rate measurements," *IEEE Trans. Microw. Theory Techn.*, vol. 57, no. 10, pp. 2498–2507, Oct. 2009.

[16] R. Fletcher and J. Han, "Low-cost differential front-end for doppler radar vital sign monitoring," in *IEEE MTT-S Int. Microw. Symp. Dig.*, 2009, pp. 1325–1328.

[17] O. Kaltiokallio, H. Yiğitler, R. Jäntti, and N. Patwari, "Non-invasive respiration rate monitoring using a single COTS TX-RX pair," in *Proc. 13th Int. Symp. Inf. Process. Sensor Netw. (IPSN)*, 2014, pp. 59–69.

[18] N. Patwari, L. Brewer, Q. Tate, O. Kaltiokallio, and M. Bocca, "Breathfinding: A wireless network that monitors and locates breathing in a home," *IEEE J. Sel. Topics Signal Process.*, vol. 8, no. 1, pp. 30–42, Feb. 2013.

[19] L. Ma, M. Liu, H. Wang, Y. Yang, N. Wang, and Y. Zhang, "WallSense: Device-free indoor localization using wall-mounted UHF RFID tags," *Sensors*, vol. 19, no. 1, p. 68, 2019.

[20] Y. Ma, Y. Zhang, B. Wang, and W. Ning, "SCLA-RTI: A novel device-free multi-target localization method based on link analysis in passive UHF RFID environment," *IEEE Sensors J.*, vol. 21, no. 3, pp. 3879–3887, Feb. 2021.

[21] Y. Ma, B. Wang, X. Gao, and W. Ning, "The gray analysis and machine learning for device-free multitarget localization in passive UHF RFID environments," *IEEE Trans. Ind. Informat.*, vol. 16, no. 2, pp. 802–813, Feb. 2020.

[22] H. Ermert and R. Karg, "Multifrequency acoustical holography," *IEEE Trans. Sonics Ultrason.*, vol. SU-26, no. 4, pp. 279–286, Jul. 1979.

[23] M. Vossiek, Y. Magori, and H. Ermert, "An ultrasonic multielement sensor system for position invariant object identification," in *Proc. IEEE Ultrason. Symp.*, vol. 2, 1994, pp. 1293–1297.

[24] M. Younis, C. Fischer, and W. Wiesbeck, "Digital beamforming in SAR systems," *IEEE Trans. Geosci. Remote Sens.*, vol. 41, no. 7, pp. 1735–1739, Jul. 2003.

[25] M. Elsdon, M. Leach, S. Skobelev, and D. Smith, "Microwave holographic imaging of breast cancer," in *Proc. Int. Symp. Microw. Antenna Propag. EMC Technol. Wireless Commun.*, 2007, pp. 966–969.

[26] D. M. Sheen, D. L. McMakin, and T. E. Hall, "Three-dimensional millimeter-wave imaging for concealed weapon detection," *IEEE Trans. Microw. Theory Techn.*, vol. 49, no. 9, pp. 1581–1592, Sep. 2001.

[27] Y. Meng, C. Lin, J. Zang, A. Qing, and N. K. Nikolova, "General theory of holographic inversion with linear frequency modulation radar and its application to whole-body security scanning," *IEEE Trans. Microw. Theory Techn.*, vol. 68, no. 11, pp. 4694–4705, Nov. 2020.

[28] R. Miesen, F. Kirsch, and M. Vossiek, "Holographic localization of passive UHF RFID transponders," in *Proc. IEEE Int. Conf. RFID*, 2011, pp. 32–37.

[29] F. Xue, J. Zhao, and D. Li, "Precise localization of RFID tags using hyperbolic and hologram composite localization algorithm," *Comput. Commun.*, vol. 157, pp. 451–460, May 2020.

[30] H. Liu, Y. Ma, Y. Jiang, and C. Tian, "Crucial or unnecessary analysis on phase differential in holographic SAR RFID localization," *IEEE Trans. Veh. Technol.*, vol. 70, no. 2, pp. 1984–1988, Feb. 2021.

[31] F. Bernardini *et al.*, "Robot-based indoor positioning of UHF-RFID tags: The SAR method with multiple trajectories," *IEEE Trans. Instrum. Meas.*, vol. 70, pp. 1–15, Oct. 2020.

[32] X. Liang, Z. Huang, S. Yang, and L. Qiu, "E3DinSAR: 3-D localization of RFID-tagged objects based on interference synthetic apertures," *IEEE Internet Things J.*, vol. 7, no. 12, pp. 11656–11666, Dec. 2020.

[33] L. Yang, Y. Chen, X.-Y. Li, C. Xiao, M. Li, and Y. Liu, "TagoRam: Real-time tracking of mobile RFID tags to high precision using cots devices," in *Proc. 20th Annu. Int. Conf. Mobile Comput. Netw.*, 2014, pp. 237–248.

[34] L. Shangguan and K. Jamieson, "The design and implementation of a mobile RFID tag sorting robot," in *Proc. 14th Annu. Int. Conf. Mobile Syst. Appl. Services*, 2016, pp. 31–42.

[35] C. A. Balanis and P. I. Ioannides, "Introduction to smart antennas," *Synth. Lectures Antennas*, vol. 2, no. 1, pp. 1–175, 2007.

[36] X. He, J. Zhu, W. Su, and M. M. Tentzeris, "RFID based non-contact human activity detection exploiting cross polarization," *IEEE Access*, vol. 8, pp. 46585–46595, 2020.

[37] Y. He, C. Gu, H. Ma, J. Zhu, and G. V. Eleftheriades, "Miniaturized circularly polarized doppler radar for human vital sign detection," *IEEE Trans. Antennas Propag.*, vol. 67, no. 11, pp. 7022–7030, Nov. 2019.

[38] Y. Dong, H. Toyao, and T. Itoh, "Compact circularly-polarized patch antenna loaded with metamaterial structures," *IEEE Trans. Antennas Propag.*, vol. 59, no. 11, pp. 4329–4333, Nov. 2011.

[39] S. Chen, S. Zhong, S. Yang, and X. Wang, "A multiantenna RFID reader with blind adaptive beamforming," *IEEE Internet Things J.*, vol. 3, no. 6, pp. 986–996, Dec. 2016.

Aline Eid (Student Member, IEEE) received the B.Eng. degree in electrical and computer engineering from Notre Dame University, Louaize, Lebanon, in 2015, and the M.S. degree in electrical and computer engineering from the American University of Beirut, Beirut, Lebanon, in 2017. She is currently pursing the Ph.D. degree in electrical engineering with the ATHENA Group (led by Prof. M. Tentzeris), Georgia Institute of Technology, Atlanta, GA, USA.

She was a Hardware Engineering Intern with the Wireless Hardware Group, Google LLC, Mountain View, CA, USA from June to December 2020. During her Ph.D., she was a recipient of more than 12 awards, inventor in four patents, and author/co-author of more than 30 conference and journal papers and book chapters. Her research interests are in electromagnetics and microwave/millimeter-wave devices and systems, intelligent, autonomous, human-aware systems and communications and networking, and zero-power mm-wave-enabled solutions for smart environments and autonomous robots and vehicles.

Ms. Eid was a recipient of the NSF travel and best paper awards at the 2018 IEEE NMDC conference, travel award and honorable mention in the student paper competition at the 2019 IEEE APS/URSI conference. At the 2019 IEEE IMS conference, she won the first place in the RFID student design competition, a second place and audience choice in the 3MT competition and an honorable mention in the student paper competition. She is also the recipient of the 2020 IEEE MTT-S graduate fellowship and Tom Brazil awards and the first-place award in the student poster competition at the 2020 FLEX MEMS Sensors Technical Congress.

Jiang Zhu (Senior Member, IEEE) received the B.S. degree in electrical engineering from Zhejiang University, Hangzhou, China, in 2003, the M.A.Sc. degree in electrical engineering from McMaster University, Hamilton, ON, Canada, in 2006, and the Ph.D. degree in electrical engineering from the University of Toronto, Toronto, ON, Canada, in 2010.

From 2010 to 2014, he was a Senior Hardware Engineer with Apple Inc., Cupertino, CA, USA. From 2014 to 2016, he was with Google[x] Life Science, and then Verily Life Science, a subsidiary of Alphabet Inc., Mountain View, CA, USA. He is currently managing the Wireless Hardware Group for Emerging Wearables, Virtual Reality and Augmented Reality Technologies and Projects with Google LLC, Mountain View, CA, USA. He has published scientific results in *Physical Review Letters*, the IEEE TRANSACTIONS ON ANTENNAS AND PROPAGATION, the IEEE TRANSACTIONS ON MICROWAVE THEORY AND TECHNIQUES, IEEE ACCESS, the IEEE ANTENNAS AND WIRELESS PROPAGATION LETTERS, *IET Microwaves*, *Antennas Propagation*, and *Electronic Letters*. He holds nearly 60 granted/filed U.S. patents, many of which have been commercialized in Apple and Google's products. His research interests include antenna design for industry applications, RF-based sensing, and the Internet of Things.

Dr. Zhu was a recipient of the IEEE Microwave Theory and Techniques Society Outstanding Young Engineer Award and the IEEE Antennas and Propagation Society Doctoral Research Award. He has been an Associate Editor for the IEEE INTERNET OF THINGS JOURNAL, the IEEE TRANSACTIONS ON ANTENNAS AND PROPAGATION, the IEEE ANTENNAS AND WIRELESS PROPAGATION LETTERS, and *IET Microwaves, Antennas, and Propagation*. He is also the Guest Editor for the IEEE Communications Magazine Special Feature Topic on Antenna Systems for 5G and Beyond. He is a member of the IEEE AP-S Industrial Initiatives Committee, the IEEE AP-S Young Professional Committee, a member and industry liaison of the IEEE AP-S Membership and Benefits Committee, a member of the IEEE MTT-S Technical Coordination Future Directions Committee—IoT Working Group, and a member of the IEEE MTT-26 RFID, Wireless Sensors, and IoT Committee. He serves on TPC and TPRC for numerous conferences, including IEEE APS, IMS, and RWS.

Luzhou Xu (Senior Member, IEEE) received the B.Eng. and M.S. degrees in electrical engineering from Zhejiang University, Hangzhou, China, in 1996 and 1999, respectively, and the Ph.D. degree in electrical and computer engineering from the University of Florida, Gainesville, FL, USA, in 2006.

From 1999 to 2019, he has been with ZTE, Shanghai, China; Philips Research, Shanghai, China; ArrayComm, San Jose, CA, USA; University of Florida; Integrated Adaptive Applications Inc., Gainesville, FL, USA; FutureWei Technologies, San Diego, CA, USA; and Amazon, San Diego, CA, USA. He is currently working with Google ATAP, Mountain View, CA, USA. His research interests include signal processing, machine learning and their applications.

Jimmy G. D. Hester received the M.S. and Ph.D. degrees in electrical and computer engineering from the Georgia Institute of Technology, Atlanta, GA, USA, in 2014 and 2019, respectively.

He is currently a Co-Founder with Atheraxon, Atlanta, GA, USA, the company commercializing the 5G RFID technology. He has been developing solutions for the use of carbon nanomaterials as well as optimized RF structures toward the implementation of inkjet-printed flexible low-cost ubiquitous gas sensors for Internet of Things and smart skin applications. His work covers the entire development process, from the development of inkjet inks, improvement of fabrication methods, sensor component design, high frequency characterization and environmental testing to the design, simulation and fabrication of the RF system embedding the sensor, and the development of wireless reading and data processing schemes. His research interests lie at the interface between radio frequency and mm-wave engineering and material science, in the form of flexible electronics technologies and nanotechnologies.

Dr. Hester was awarded the 2015 NT4D Student Award, a Second Place Best Poster Award at the 2017 IEEE Futurecar conference, a Third Place Best Poster Award at the 2017Flex conference, and a Honorable Mention Award as finalist of the 2017 IMS student paper competition.

Manos M. Tentzeris (Fellow, IEEE) received the Diploma degree (*magna cum laude*) in electrical and computer engineering from the National Technical University of Athens, Athens, Greece, in 1992, and the M.S. and Ph.D. degrees in electrical engineering and computer science from the University of Michigan, Ann Arbor, MI, USA, in 1994 and 1998, respectively.

He is currently Ken Byers Professor in flexible electronics with the School of Electrical and Computer Engineering, Georgia Institute of Technology, Atlanta, GA, USA, where he heads the ATHENA Research Group (20 Researchers). He has served as the Head of the GT ECE Electromagnetics Technical Interest Group, as the Georgia Electronic Design Center Associate Director of RFID/Sensors Research, as the Georgia Institute of Technology NSF-Packaging Research Center Associate Director of RF Research, and as the RF Alliance Leader. He was a Visiting Professor with the Technical University of Munich, Munich, Germany, in 2002, with GTRI-Ireland, Athlone, Ireland, in 2009, and with LAAS-CNRS, Toulouse, France, in 2010. He has helped develop academic programs in 3-D/inkjet-printed RF electronics and modules, flexible electronics, origami and morphing electromagnetics, highly integrated/multilayer packaging for RF and wireless applications using ceramic and organic flexible materials, paper-based RFID's and sensors, wireless sensors and biosensors, wearable electronics, "Green" electronics, energy harvesting and wireless power transfer, nanotechnology applications in RF, microwave MEMs, and SOP-integrated (UWB, multiband, mmW, and conformal) antennas. He has authored over 850 papers in refereed journals and conference proceedings, six books, and 27 book chapters.

Dr. Tentzeris was a recipient/co-recipient of the 2019 Humboldt Research Prize, the 2017 Georgia Institute of Technology Outstanding Achievement in Research Program Development Award, the 2016 Bell Labs Award Competition 3rd Prize, the 2015 IET Microwaves, Antennas, and Propagation Premium Award, the 2014 Georgia Institute of Technology ECE Distinguished Faculty Achievement Award, the 2014 IEEE RFID-TA Best Student Paper Award, the 2013 IET Microwaves, Antennas and Propagation Premium Award, the 2012 FiDiPro Award in Finland, the iCMG Architecture Award of Excellence, the 2010 IEEE Antennas and Propagation Society Piergiorgio L. E. Uslenghi Letters Prize Paper Award, the 2011 International Workshop on Structural Health Monitoring Best Student Paper Award, the 2010 Georgia Institute of Technology Senior Faculty Outstanding Undergraduate Research Mentor Award, the 2009 IEEE TRANSACTIONS ON COMPONENTS AND PACKAGING TECHNOLOGIES Best Paper Award, the 2009 E. T. S. Walton Award from the Irish Science Foundation, the 2007 IEEE AP-S Symposium Best Student Paper Award, the 2007 IEEE MTT-S IMS Third Best Student Paper Award, the 2007 ISAP 2007 Poster Presentation Award, the 2006 IEEE MTT-S Outstanding Young Engineer Award, the 2006 Asia–Pacific Microwave Conference Award, the 2004 IEEE TRANSACTIONS ON ADVANCED PACKAGING Commendable Paper Award, the 2003 NASA Godfrey "Art" Anzic Collaborative Distinguished Publication Award, the 2003 IBC International Educator of the Year Award, the 2003 IEEE CPMT Outstanding Young Engineer Award, the 2002 International Conference on Microwave and Millimeter-Wave Technology Best Paper Award (Beijing, China), the 2002 Georgia Institute of Technology—ECE Outstanding Junior Faculty Award, the 2001 ACES Conference Best Paper Award, the 2000 NSF CAREER Award, and the 1997 Best Paper Award of the International Hybrid Microelectronics and Packaging Society. He was the TPC Chair of the IEEE MTT-S IMS 2008 Symposium and the Chair of the 2005 IEEE CEM-TD Workshop. He is the Vice-Chair of the RF Technical Committee (TC16) of the IEEE CPMT Society. He is the Founder and Chair of the RFID Technical Committee (TC24) of the IEEE MTT-S and the Secretary/Treasurer of the IEEE C-RFID. He is an Associate Editor of the IEEE TRANSACTIONS ON MICROWAVE THEORY AND TECHNIQUES, the IEEE TRANSACTIONS ON ADVANCED PACKAGING, and the *International Journal on Antennas and Propagation*. He has given over 100 invited talks to various universities and companies all over the world. He is a member of the URSI-Commission D and the MTT-15 Committee, an Associate Member of EuMA, a Fellow of the Electromagnetic Academy, and a member of the Technical Chamber of Greece. He served as one of the IEEE MTT-S Distinguished Microwave Lecturers from 2010 to 2012 and is one of the IEEE CRFID Distinguished Lecturers.